AGU100 ADVANCING EARTH AND SPACE SCIENCE

Water Resources Research

RESEARCH ARTICLE
10.1029/2018WR023067

Key Points:
- Drone information on riverbed topography and hydraulic head data provide useful information for the simulation of river-aquifer systems
- Parameter estimation via data assimilation allows better estimation of hydraulic heads and slightly better estimation of river discharge

Supporting Information:
- Supporting Information S1
- Data Set S1
- Data Set S2
- Data Set S3
- Data Set S4
- Data Set S5
- Data Set S6
- Data Set S7
- Data Set S8

Correspondence to:
Q. Tang,
qi.tang@awi.de

Citation:
Tang, Q., Schilling, O. S., Kurtz, W., Brunner, P., Vereecken, H., & Hendricks Franssen, H.-J. (2018). Simulating flood-induced riverbed transience using unmanned aerial vehicles, physically based hydrological modeling, and the ensemble Kalman filter. *Water Resources Research*, *54*, 9342–9363. https://doi.org/10.1029/2018WR023067

Received 5 APR 2018
Accepted 29 OCT 2018
Accepted article online 6 NOV 2018
Published online 23 NOV 2018

Simulating Flood-Induced Riverbed Transience Using Unmanned Aerial Vehicles, Physically Based Hydrological Modeling, and the Ensemble Kalman Filter

Qi Tang[1,2,3], Oliver S. Schilling[4,5], Wolfgang Kurtz[1,2,6], Philip Brunner[4], Harry Vereecken[1,2], and Harrie-Jan Hendricks Franssen[1,2]

[1]Institute for Bio- and Geosciences: Agrosphere (IBG-3), Forschungszentrum Jülich GmbH, Jülich, Germany, [2]Centre for High-Performance Scientific Computing in Terrestrial Systems, HPSC TerrSys, Geoverbund ABC/J, Jülich, Germany, [3]Now at Alfred Wegener Institute, Helmholtz Centre for Polar and Marine Research, Bremerhaven, Germany, [4]Centre for Hydrogeology and Geothermics, University of Neuchâtel, Neuchâtel, Switzerland, [5]Department of Geology and Geological Engineering, Université Laval, Pavillon Adrien-Pouliot, Québec, Québec, Canada, [6]Leibniz Supercomputing Centre, Environmental Computing Group, Garching bei München, Germany

Abstract Flood events can change the riverbed topography as well as the riverbed texture and structure, which in turn can influence the riverbed hydraulic conductivity (K_{rb}) and river-aquifer exchange fluxes. A major flood event occurred in the Emme River in Switzerland in 2014, with major implications for the riverbed structure. The event was simulated with the fully integrated hydrological model HydroGeoSphere. The aim was to investigate the effect of the spatial and temporal variability of riverbed topography and K_{rb} on predictions of hydraulic states and fluxes and to test whether data assimilation (DA) based on the ensemble Kalman filter (EnKF) can better reproduce flood-induced changes to hydraulic states and parameters with the help of riverbed topography changes recorded with an unmanned aerial vehicle (UAV) and through-water photogrammetry. The performance of DA was assessed by evaluating the reproduction of the hydraulic states for the year 2015. While the prediction of surface water discharge was not affected much by the changes in riverbed topography and in K_{rb}, using the UAV-derived postflood instead of the preflood riverbed topography reduced the root-mean-square error of predicted heads (RMSE [*h*]) by 24%. If, in addition to using the postflood riverbed topography, also K_{rb} and aquifer hydraulic conductivity (K_{aq}) were updated through DA after the flood, the RMSE (*h*) was reduced by 55%. We demonstrate how updating of K_{rb} and K_{aq} based on EnKF and UAV-based observations of riverbed topography transience after a major flood event strongly improve predictions of postflood hydraulic states.

1. Introduction

The riverbed plays a key role for modeling river-aquifer interactions (e.g., Brunner et al., 2017; Mattle et al., 2001; Partington et al., 2017; Schilling, Gerber, et al., 2017). When a riverbed is considered within a hydrological flow model, both riverbed topography and the riverbed hydraulic conductivity (K_{rb}) are critical variables to be quantified. Riverbed topography constitutes a key control for surface water-groundwater (SW-GW) exchange fluxes (Cardenas, 2009; Harvey & Bencala, 1993; Hester & Doyle, 2008; Kasahara & Wondzell, 2003; Shope et al., 2012; Tonina & Buffington, 2007; Woessner, 2000; J. Zhang et al., 2017). It is also important for numerous biogeochemical processes in the hyporheic zone (Boano et al., 2010; Harvey et al., 2012; Marzadri et al., 2014; Wildhaber et al., 2014). Boano et al. (2010) found that nutrient concentrations and organic carbon degradation were strongly influenced by the streambed morphology. Nitrous oxide emissions from rivers were highly related to the streambed geomorphologic characteristics and sediment properties (Marzadri et al., 2014). Wildhaber et al. (2014) found that fine sediment and streambed morphology also affected oxygen and water exchange. K_{rb} also plays an important role in the dynamics of exchange fluxes and solute transport processes between the river and the surrounding GW system (e.g., Cardenas et al., 2004; Irvine et al., 2012; Kalbus et al., 2009; Käser et al., 2009; Lackey et al., 2015; Miller et al., 2016; Ryan & Boufadel, 2006; Song et al., 2007; Song et al., 2016; Woessner, 2000).

Riverbed topography, as well as its texture and materials, may change in time and space due to erosion and deposition processes across the river-aquifer interface (e.g., Birck, 2006; Doppler et al., 2007; Mutiti & Levy, 2010; Schubert, 2006; Simpson & Meixner, 2012). This also causes changes to K_{rb} and thus to SW-GW fluxes (Doppler et al., 2007; Grischek & Bartak, 2016; Nowinski et al., 2011; Ulrich et al., 2015). Both measurements from field and laboratory experiments as well as results from numerical flow models provide evidence of this: Birck (2006) explored the impact of high river stages on scouring of the riverbed and the corresponding changes of K_{rb} along the Great Miami River at Charles M. Bolton Water Plant in southwest Ohio, USA. A scouring of up to 0.06 m and a total fluctuation of 0.17 m were detected during the flood in January 2005. However, the contribution of scouring to the variation of overall K_{rb} was minimal. Schubert (2006) observed a highly dynamic clogging process and a significant temporal variation in the permeability of the clogged layer with rising and lowering water level in the lower Rhine region, Germany. Doppler et al. (2007) provided field evidence of temporally varying leakage coefficients playing an important role when simulating GW flow for the upper Limmat valley in Zürich, Switzerland. The GW flow model needed to be recalibrated after a flood event, as the infiltration rate from the river into the aquifer was increased due to the flood-induced erosion and the corresponding increase in K_{rb}. Mutiti and Levy (2010) investigated the temporal evolution of K_{rb} during a storm event beginning on 12 June 2005 at Charles M. Bolton Water Plant in southwest Ohio, USA. GW flow and heat transport were simulated with the model VS2DHI (Hsieh et al., 2000). An increase of K_{rb} by almost 1 magnitude was observed due to the loss of fine materials during the scouring process. Nowinski et al. (2011) observed temporally varying K_{rb} on a riverbed point bar at the meander scale throughout the period of 1 year; originally high K_{rb} decreased due to the accumulation of fine materials transported by the river. Simpson and Meixner (2012) used a series of SW and GW flow models to simulate a synthetic flood event and its effect on K_{rb} and SW-GW interactions. The total amount of scouring and filling was 12 and 16 mm, respectively, relatively small compared to the flood flow rate. Ulrich et al. (2015) investigated the spatiotemporal variability of riverbed permeability and the mechanisms behind it by monitoring the clogging process with different methods at the Russian River near Forestville, California, from May to November in 2012. A decrease of permeability was observed from the onset of September due to the formation and accumulation of biomass on the riverbed. Gianni et al. (2016) developed a method to identify changes in the hydraulic properties of riverbeds by analyzing head changes in the river and a nearby piezometer. The method was applied to the Rhone river, and changes of 2 orders of magnitude were identified. Grischek and Bartak (2016) reviewed and documented the temporal variation of the ratio between K_{rb} and clogging layer thickness from 1971 to 2015 for the Elbe River in Germany. The results from the field tests showed that the leakage coefficient increased by a factor of 1.3 to 3.3 during the observed period.

The findings of the reviewed studies make it evident that it is important to characterize the spatiotemporal variation of K_{rb} and riverbed topography induced by a flood, as well as the corresponding dynamic influence on the hydraulic states and fluxes of the river-aquifer system. However, transient changes in K_{rb} and riverbed topography are rarely observed and considered in hydrological models, and studies focusing on riverbed transience had until now either a focus on data collection or were based on synthetic studies. Real-world modeling studies, in which the riverbed is explicitly considered, treat riverbed topography and K_{rb} in general as static properties, with the exception of a very small number of studies (Kurtz et al., 2012; Mutiti & Levy, 2010; Y. Zhang et al., 2011).

Where flood-induced changes were not observed directly, indirect methods such as inverse modeling may provide a solution to estimate the changes to riverbed topography and structure retrospectively. However, it has not been shown for a real-world case whether such an approach is able to reproduce transience in riverbed properties and improve simulation results by taking this transience into account. Data assimilation (DA) is one possible inverse modeling method for this purpose (Chen & Zhang, 2006; Hendricks Franssen & Kinzelbach, 2008). Until now DA has already been successfully applied for estimating K_{rb} in several cases (e.g., Alzraiee et al., 2017; Hendricks Franssen et al., 2011; Kurtz et al., 2012; Kurtz et al., 2013; Kurtz et al., 2014; Tang et al., 2015; Tang et al., 2017). Hendricks Franssen et al. (2011) estimated leakage coefficients for a limited number of zones together with aquifer hydraulic conductivity (K_{aq}), using a 3-D variably saturated GW flow model of the Limmat valley, Switzerland. The prediction of hydraulic heads was improved, if both parameters were updated using the ensemble Kalman filter (EnKF). Kurtz et al. (2012) successfully captured the spatial and temporal variation of K_{rb} for a synthetic 3-D river-aquifer model with joint updating of piezometer heads and K_{rb} by EnKF. Later, the importance of K_{rb} spatial

heterogeneity in the Limmat valley river-aquifer system was studied by Kurtz et al. (2013). The heterogeneous K_{rb} as well as the piezometric heads can be even better estimated when both GW temperature data and piezometric heads are assimilated (Kurtz et al., 2014). Tang et al. (2015) investigated the impact of different K_{rb} patterns on the estimation of hydraulic heads, K_{rb}, and river-aquifer exchange fluxes for a synthetic experiment with a 3-D conductance based GW model. The SW heads are predefined as fixed head boundary and exchange fluxes between the river and the aquifer are calculated according to Darcy's law. Using this kind of flow model approach, it was found that complex K_{rb} patterns did not have a significant influence on the characterization of river-aquifer exchange fluxes. This was further explored by Tang et al. (2017) using a physically based, fully integrated SW-GW model able to simulate variably saturated conditions. Under fully saturated conditions, results were consistent with those shown in Tang et al. (2015); under variably saturated conditions, however, the histogram of K_{rb} provided useful additional information for the characterization of net river-aquifer exchange fluxes, suggesting that the pattern of K_{rb} is nevertheless important. Alzraiee et al. (2017) successfully estimated spatially varying K_{rb} and K_{aq} by assimilating GW-level measurements using the ensemble smoother. The study included a verification of the estimated parameter distributions, for both a synthetic experiment and a real-world system. The verification was based on simulated GW levels, streamflow rates, and flow exchange between the stream and the aquifer.

Whether riverbed topogaphy and K variations during and after a flood event can be reproduced from hydraulic head data by an inverse modeling approach is still unknown. Moreover, the importance of riverbed topography and K_{rb} variations for the prediction of hydraulic heads and of fluxes between the river and the aquifer is also still unknown. We therefore aim at answering these questions with a combination of (1) observations of riverbed topography and structure changes induced by a major flood event using unmanned aerial vehicles (UAVs), (2) fully integrated and physically based flow modeling, and (3) DA. With the integration of these state-of-the-art techniques, we characterize the spatially and temporally varying riverbed properties induced by a major flood event and analyze their impacts on the prediction of hydraulic heads, SW discharge, and river-aquifer exchange fluxes. A 3-D river-aquifer flow model of the Emme valley (Switzerland) was set up for this purpose, using the physically based, fully integrated SW-GW flow model HydroGeoSphere (HGS). With this 3-D river-aquifer flow model, the hydraulic response to a major flood event was simulated. Two high-resolution data sets of riverbed topography obtained using an UAV before and one after the flood event were used to define the riverbed topography in the model. To our knowledge, this is one of the first works where flood-related changes in riverbed topography are detected by UAV before and after a flood, and this information is used in a modeling context. Ensembles of different heterogeneous K_{aq} and K_{rb} fields were generated using sequential Gaussian simulations and served as input for the hydrological flow model. DA experiments were carried out using the EnKF. The DA experiments were designed to systematically answer the following questions:

1. Assuming that only information on the riverbed topography is available for the preflood and postflood period but no hydraulic information: Does a change in riverbed topography have an influence on hydraulic heads, SW discharge, and river-aquifer exchange fluxes, and is it important to consider this change in hydrological modeling?
2. Assuming that measurements of hydraulic heads are available for the preflood and postflood period but no information on the postflood riverbed topography: Can DA of the hydraulic head measurements of the preflood period allow calibrating the aquifer and K_{rb} sufficiently well so that the hydraulic heads and river discharge of the postflood period can be reproduced? Moreover, if K_{aq} and K_{rb} are continuously updated through DA, but the riverbed topography remains unchanged, can the parameters update through DA compensate for the missing riverbed topography and produce as good results as when the correct (postflood) riverbed topography would be used?
3. Assuming that both hydraulic head measurements and riverbed topography information are available for the preflood and postflood period**:** How fast can DA based on EnKF adapt K_{aq} and K_{rb} using information of hydraulic heads and riverbed topography?
4. Does the correct estimation of K_{aq} or the correct estimation of K_{rb} play a more important role for the simulation of exchange fluxes? How does this change, if information on the flood-induced changes to the riverbed topography is available?

2. Materials and Methods

2.1. Integrated Hydrological Model HGS

HGS (Aquanty Inc, 2016; Brunner & Simmons, 2012; Therrien et al., 2010) is a physically based, fully integrated hydrological model designed for accounting for all components in the water cycle. The SW and GW flow equations are solved simultaneously. HGS has been used for the simulation of many different hydrological systems, for example, for the interactions between GW, SW and vegetation (e.g., Ala-aho et al., 2017; Banks et al., 2011; Schilling et al., 2014; Schomburg et al., 2018), for the detection of the sensitivity of catchment scale dynamics to the different model parameters (Cornelissen et al., 2016), to track catchment scale SW levels and overland flow routing (Ameli & Creed, 2017), to explore the hydrological dynamics of wetlands (Liu et al., 2016) and microtopographic wetland runoff (Frei et al., 2010), and for large-scale solute transport (Blessent et al., 2011). In a few instances HGS was calibrated against different types of data (e.g., Brunner et al., 2012; Karan et al., 2014; Schilling et al., 2014; Schilling, Gerber, et al., 2017) using the automatic inverse code PEST (Doherty, 2015). Recently, HGS has been coupled to a sequential DA routine (EnKF-HGS) by Kurtz et al. (2017).

SW flow is described by the two-dimensional Saint Venant equation:

$$\frac{\partial \varphi_0 h_0}{\partial t} = -\nabla \cdot d_0 \mathbf{q_0} - d_0 \Gamma \pm Q_0 \tag{1}$$

where φ_0 is the surface flow domain porosity (−), h_0 is the SW elevation (L), d_0 is the SW depth (L), Γ is the exchange flow rate ($L^3 \cdot L^{-2} \cdot T^{-1}$) between the surface domain and the subsurface domain, Q_0 is external sources and sinks (L/T), and $\mathbf{q_0}$ is the fluid flux (L/T) given by

$$\mathbf{q_0} = -\mathbf{K_0} \cdot k_{r0} \nabla (d_0 + z) \tag{2}$$

where $\mathbf{K_0}$ is surface conductance (L/T) of the Manning's equation and k_{r0} accounts for the for the additional resistance in horizontal conductance caused by obstruction storage, varying between 0 and 1.

GW flow is implemented by the three-dimensional Richards' equation:

$$\frac{\partial}{\partial t}(\theta_s s_w) = -\nabla \cdot \mathbf{q} + \Gamma \pm Q \tag{3}$$

where θ_s is the saturated soil water content (−), s_w is the degree of water saturation (−), $\mathbf{q}$ is the Darcy flux (L/T), Γ is the volumetric fluid exchange rate ($L^3 \cdot L^{-2} \cdot T^{-1}$) between the surface domain and the subsurface domain, and Q are sinks and sources ($L^3 \cdot L^{-2} \cdot T^{-1}$). The dual-node approach is used for the flow coupling between the surface and the subsurface domain (see de Rooij, 2017). Van Genuchten (1980) functions are used to describe the relationship between the hydraulic conductivity of the porous medium, the soil water content, and pressure.

2.2. EnKF

DA is done using the EnKF in this study (Evensen, 1994). EnKF was originally developed for the estimation of system states and was later extended for the estimation of parameters (Chen & Zhang, 2006; Hendricks Franssen & Kinzelbach, 2008). Parameter estimates are successful only if a strong correlation exists between the assimilated system-response variables and the parameters. The following description contains the EnKF algorithm as it is coupled to HGS:

EnKF consists of three basic equations: the forecast equation, the observation equation, and the updating equation. Being a Monto Carlo based inverse modeling method, EnKF uses a (large) number of stochastic realizations of model states and parameters to represent the model uncertainties. The augmented state vector includes both the model states and model parameters. For each stochastic realization, the augmented state vector can be written as

$$\mathbf{x}_i = \begin{pmatrix} \mathbf{x}_s \\ \mathbf{x}_p \end{pmatrix}_i \tag{4}$$

where $\mathbf{x}_s$ is the vector with model states and $\mathbf{x}_p$ is the vector of model parameters. The subscript i is the realization number. In this study, the augmented state vector contains one type of state variable (hydraulic head) and one type of model parameter (log-transformed hydraulic conductivity):

$$\mathbf{x}_i = \begin{pmatrix} \mathbf{h} \\ \log_{10}(\mathbf{K}) \end{pmatrix}_i \tag{5}$$

where **h** is hydraulic head and **K** hydraulic conductivity. Here **K** can include K_{rb}, K_{aq}, or both, depending on the assimilation scenario.

The model states at the current time step are predicted from the previous time step using HGS according the forecast equation:

$$\mathbf{x}_{t,i} = M\left(\mathbf{x}_{t-1,i}\right) \tag{6}$$

where M is the forward hydrological model and the subscript t represents the time step.

The observations available at time step t are perturbed according to the observation equation:

$$\mathbf{y}_{t,i} = \mathbf{y}_t + \boldsymbol{\varepsilon}_{t,i} \tag{7}$$

where $\mathbf{y}_{t,\,i}$ is the vector of perturbed measurements, $\mathbf{y}_t$ is the vector with original measurements at time step t, and $\boldsymbol{\varepsilon}_{t,\,i}$ is the vector with observation errors usually generated from a normal distribution with 0 mean and standard deviation equal to the measurement error.

Combining the model prediction with the observations, the state vector is updated according the following updating equation:

$$\mathbf{x}^a_{t,i} = \mathbf{x}^f_{t,i} + \alpha\mathbf{G}\left(\mathbf{y}_{t,i} - \mathbf{H}\mathbf{x}^f_{t,i}\right) \tag{8}$$

where $\mathbf{x}^a_{t,i}$ is the augmented state vector containing the updated model states and parameters, $\mathbf{x}^f_{t,i}$ is the vector with the forecasted states obtained from the hydrological model, α is a damping factor varying between 0 and 1 (in this study α is 0.1 for parameters and 1 for states), **H** is the measurement operator matrix mapping the simulated states to the observation locations, and **G** is the Kalman gain, which weights the relative importance of the model forecasts and the observations. The Kalman gain is calculated by

$$\mathbf{G} = \mathbf{C}\mathbf{H}^T\left(\mathbf{H}\mathbf{C}\mathbf{H}^T + \mathbf{R}\right)^{-1} \tag{9}$$

where **R** is a diagonal covariance matrix representing the measurement errors at individual observation locations (this matrix is in this study a priori defined based on knowledge about the precision of instruments) and **C** is the covariance matrix of the model states and parameters, given by

$$\mathbf{C} = \begin{pmatrix} \mathbf{C}_{\mathbf{h},\mathbf{h}} & \mathbf{C}_{\mathbf{h},\log_{10}\mathbf{K}} \\ \mathbf{C}_{\log_{10}\mathbf{K},\mathbf{h}} & \mathbf{C}_{\log_{10}\mathbf{K},\log_{10}\mathbf{K}} \end{pmatrix} \tag{10}$$

where the submatrix $\mathbf{C}_{\mathbf{h},\log_{10}\mathbf{K}}$ is calculated by

$$\mathbf{C}_{\mathbf{h},\log_{10}\mathbf{K}} = \frac{1}{N-1}\sum_{i=1}^{N}\left(x_{i,\mathbf{h}} - \overline{x}_{i,\mathbf{h}}\right)\left(x_{i,\log_{10}\mathbf{K}} - \overline{x}_{i,\log_{10}\mathbf{K}}\right) \tag{11}$$

and the overbar indicates ensemble mean.

Once the updating step is done, the updated model states and parameters will be used as input for the hydrological model for the next computation time step. Each time when observations are available, equations (4)–(7) are applied. For more technical aspects of the coupling between HGS and EnKF see Kurtz et al. (2017).

2.3. Description of the Study Site

The Upper Emme catchment in the Northern prealps of Switzerland is home to one of the largest drinking water stations of the Swiss capital Bern (Blau & Muchenberger, 1997; Käser & Hunkeler, 2016; Schilling, Irvine, et al., 2017). The Emme River, which is the primary source of recharge for the alluvial aquifer of the Upper Emme catchment, has an average annual discharge of 4.4 m^3/s and is characterized by highly

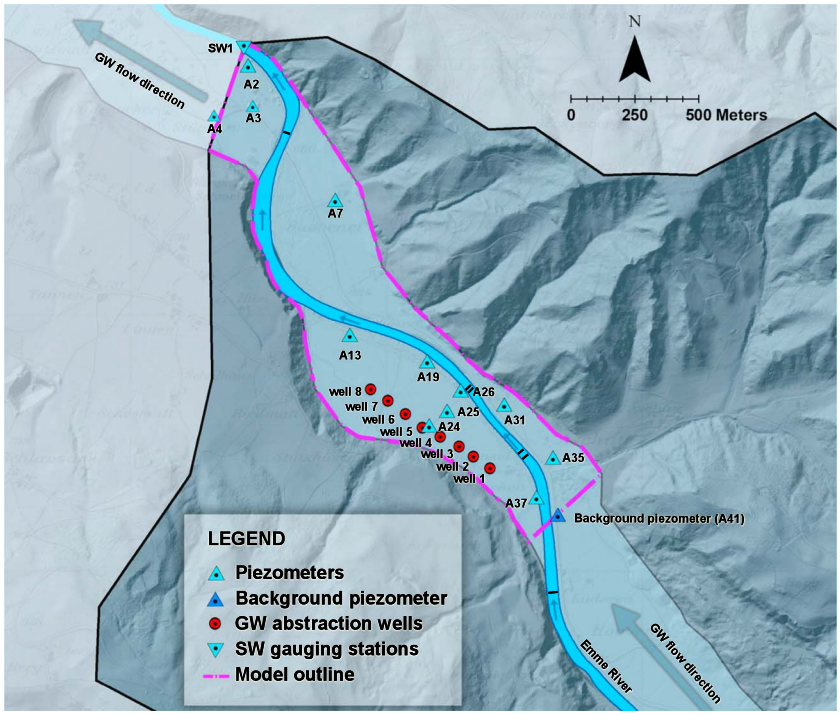

Figure 1. Location of the measurement stations of hydraulic heads and surface water discharge within the study site.

dynamic discharge behavior (Käser & Hunkeler, 2016). The drinking water station is situated on the valley bottom toward the outlet of the catchment at an elevation of 690 m above sea level (Figure 1). At that location, the topographic gradient is approximately 0.9% (Käser & Hunkeler, 2016). A total rate of 0.4 m^3/s of GW is pumped from eight wells located on a wellfield in the ultimate vicinity of the Emme River.

The unconfined alluvial aquifer, out of which the GW is pumped, is composed of highly permeable quaternary alluvial gravel (~80%) and sand (~20%) with an average hydraulic conductivity of around 4×10^{-3} m/s and is limited below by an impermeable layer of freshwater molasses (Würsten, 1991). The average thickness of the aquifer around the drinking water station is 25 m (Würsten, 1991). GW is abstracted from a depth of 10 m by the three upstream wells (wells 1–3) and from a depth of 15 m by the five downstream wells (wells 4–8) (see Figure 1). An extensive monitoring network (see Figure 1) to manage the drinking water abstraction exists (Blau & Muchenberger, 1997; Kropf et al., 2014; Lapin et al., 2014).

Multiple studies have been carried out in order to better characterize and quantify the river-aquifer interactions: Figura et al. (2013, 2015) characterized and predicted the evolution of GW temperature at the drinking water wellfield based on future climate scenarios, indicating an increasing trend. Käser and Hunkeler (2016) used temperature and electrical conductivity measurements in the Emme River to show that directly upstream of the wellfield river water is mostly infiltrating into the subsurface, whereas due to a narrowing of the aquifer downstream of the wellfield GW is exfiltrating back into the stream. Two weirs located in the Emme River at the height of the wellfield are also influencing SW-GW interactions, producing locally losing conditions upstream and locally gaining conditions downstream of the weirs. Multiple studies show that the pumping rates strongly influence SW-GW interactions around the drinking water wellfield, and this can pose a major threat both to drinking water quality as well as to the riparian ecosystem health (Blau & Muchenberger, 1997; Schilling, Irvine, et al., 2017). Schilling, Irvine, et al. (2017) carried out a multitracer study and found that the GW pumped at the drinking water wellfield contains approximately 50% older GW and 50% SW that infiltrated directly upstream of the wellfield. They showed that the key parameter controlling the SW-GW interactions of this system, and therefore mixing between recently infiltrated SW and older GW in the subsurface, is the K_{rb}. Unfortunately, the K_{rb} around the wellfield is very variable and poorly known, but the mean is estimated to be approximately 2 orders of magnitude lower than the hydraulic conductivity of the aquifer (Schilling, Irvine, et al., 2017).

2.4. UAV-Based Riverbed Topography Observations

A violent flood with a return period of only 300 years and a peak discharge of 350 m^3/s occurred on 24 July 2014 and substantially altered the riverbed topography and most likely also riverbed properties. Owing to the recent advances in UAV technology, observations of multiple aspects of rivers (e.g., riverbed topography changes and SW temperature) can now be carried out in high resolution and at comparably low costs (e.g., Feurer et al., 2008; Pai et al., 2017). The riverbed topography was recorded in high resolution (i.e., 0.25-m horizontal, 0.05-m vertical resolution) both before the flood (on 12 February 2014) and after the flood (on 20 March2015). The riverbed topography was obtained with through-water photogrammetry of remotely sensed images taken from different angles. The method was reviewed in detail by Feurer et al. (2008). A high-resolution digital elevation model (DEM) of the floodplain was available from Swisstopo (2010). Based on the two riverbed DEMs and the floodplain DEM, two DEMs of the study area around the drinking water wellfield, representing the topography before and after the flood, were generated (Figure 2). Particularly in the meander downstream of the wellfield, the average depth was reduced by the flood, and scouring moved the deep preflood channel toward the outside of the meander, whereas depositions on the inside of the meander resulted in a new gravel bank (see highlighted area of Figure 2).

3. The River-Aquifer Flow Model

3.1. Model Setup

3.1.1. Model discretization

The numerical model used for this study has been described in detail by Schilling, Irvine, et al. (2017): Vertically, the model is divided into 15 layers, and proportional sublayering is used: the top 5 layers cover each 0.61%, the following 4 layers each 6.1%, and the bottom 5 layers each 12% of the total aquifer depth, which results in 0.28-, 2.8-, and 5.5-m-thick layers at the location where the aquifer has the largest vertical extent (46 m). Horizontally, the model is discretized by equilateral triangles of 17.5-m-side length on the floodplain and 8.5-m-side length within the Emme River, resulting in 10,983 elements per layer, that is, 5,645 nodes per slice. The model outline is illustrated in Figure 1. The automatic time-stepping scheme implemented in HGS was used.

3.1.2. Model Parameterization

The riverbed was conceptualized as a slightly clogged layer within the Emme River boundaries, spanning across the four topmost model sub layers. An average K_{rb} value of 2.8×10^{-5} m/s was found to best reproduce the observed mixing ratios between older GW and freshly infiltrated SW in the wellfield (Schilling, Irvine, et al., 2017). For the aquifer, a homogeneous value of 2.9×10^{-3} m/s, which is about 2 magnitudes higher than the riverbed, is used to represent the K_{aq}. These mean K_{rb} and K_{aq} values were used as starting points for the generation of spatially distributed K_{rb} and K_{aq} fields used later in the DA experiments (described below in the section 3.2). The porosity of the aquifer layers was set to 0.15, representing a typical value of gravel-sand aquifers (Anderson et al., 2015; Fetter, 2000), and 0.41 for the riverbed layers. The unsaturated van Genuchten parameters α and β were set to 3.48/m and 1.75, respectively, representing typical values for gravel-sand aquifers according to Li et al. (2008). The residual saturation (S_{wr}) was fixed at 0.05. The coupling length (l_{exch}) between the SW and the GW domain was set to a very small value of 0.001 m, representing an optimal compromise between head continuity and numerical stability (see de Rooij, 2017).

3.1.3. Boundary Conditions

The daily changing transient boundary conditions were based on measurement time series aggregated to daily values. Precipitation was conceptualized as a second type, specified flux boundary condition, and input time series of precipitation were obtained from the nearby weather station in Langnau, that is, operated by MeteoSuisse ([lat/long]: 07°48.33′/46°56.38′, elevation [meter above sea level]: 745). Evapotranspiration was addressed by correcting the precipitation input time series with the actual evapotranspiration rate, calculated after Spreafico and Weingartner (2005), and using solar radiation and air temperature measurements of the same weather station as input. The Emme River inflow was also conceptualized as a specified flux boundary condition, and discharge input time series were obtained from two measurement stations located 5 km upstream of the upstream model boundary. The SW outflow boundary was conceptualized as a critical depth boundary condition. On the upstream boundary of the model, GW inflow was implemented as a first type, constant head boundary condition using measured GW levels from the piezometer located directly on the upstream model boundary (A41; see Figure 1). The prescribed hydraulic head underneath the riverbed

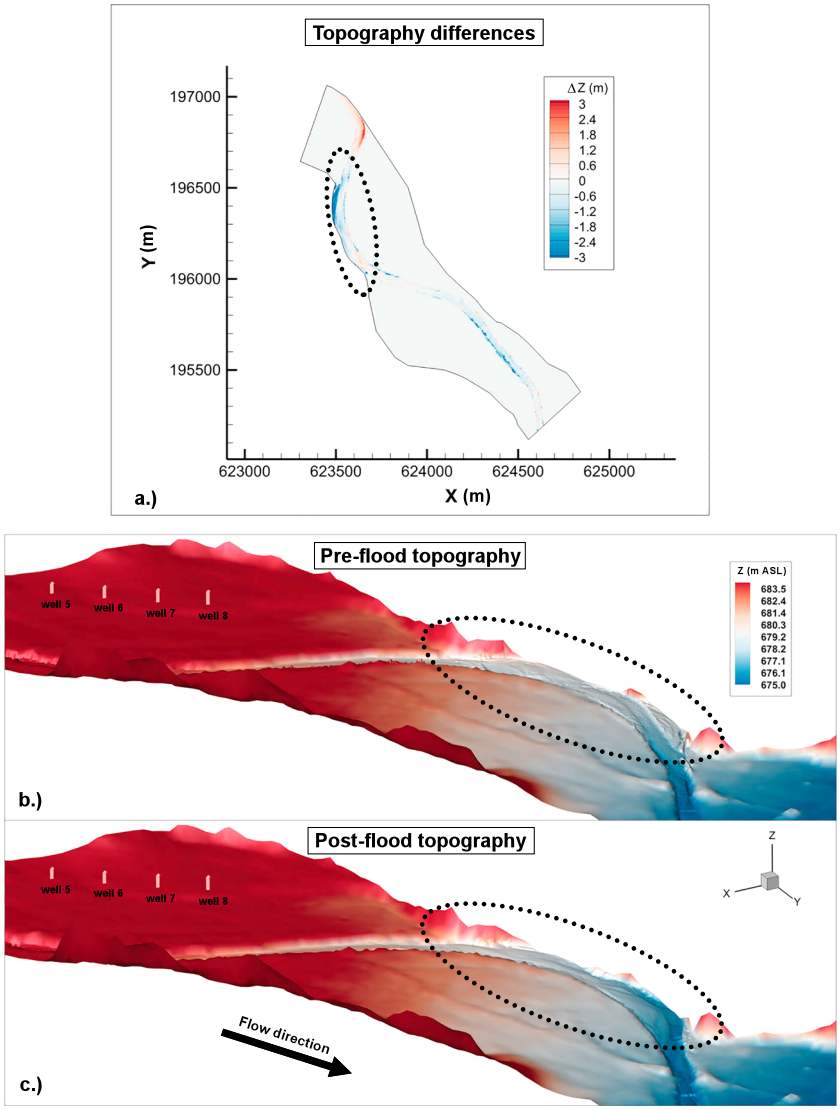

Figure 2. Illustration of the elevation differences between (a) preflood and postflood topography, as well as 3-D illustrations of the (b) preflood and the (c) postflood topographies. The meander section in which the largest changes to the riverbed topography occurred during the flood is highlighted by a dashed ellipse. Coordinates in (a) correspond to the Swiss coordinate system CH1903+/LV95.

along the upstream boundary of the model was fixed to 1 m above the hydraulic head measured in piezometer A41. This allowed accounting for mounding due to losing conditions underneath the river. For the downstream part, a constant head boundary condition was implemented and GW levels measured in a piezometer on the downstream model boundary (A3; see Figure 1) were used. The lateral model boundaries and the bottom of the model were set impermeable according to Schilling, Irvine, et al. (2017). The GW pumps of the drinking water station were implemented as single-node specified flux boundary conditions at the corresponding depth of each well. GW abstraction time series were provided by the waterworks association of the region of Bern (WVRB).

3.2. Hydraulic Conductivity Fields

Spatially heterogeneous K_{aq} and K_{rb} fields were used as input for the open loop (OL) and DA experiments. As Tang et al. (2017) demonstrated, multi-Gaussian distributed K fields provide good results for fully connected river-aquifer systems, even if K_{rb} shows non-multi-Gaussian patterns, and non-multi Gaussian K fields are not

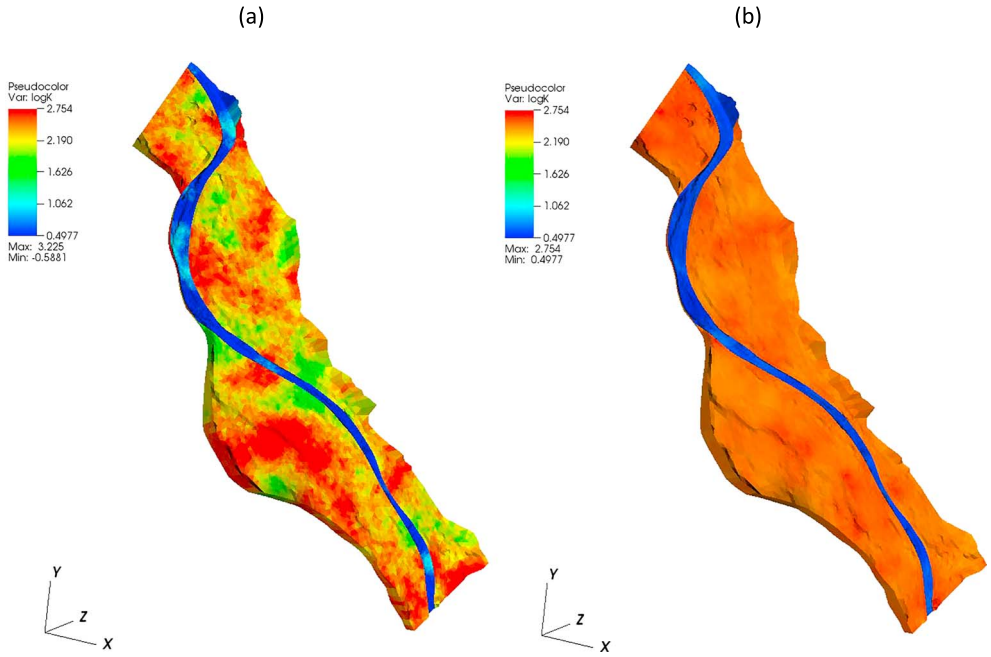

Figure 3. (a) One stochastic realization of the initial K_{aq} and K_{rb} field. (b) The ensemble mean of the initial K_{aq} and K_{rb} fields, calculated over 128 realizations.

required. We therefore used a multi-Gaussian geostatistical model for the generation of both random K_{rb} and K_{aq} fields. The generated random K_{rb} and K_{aq} fields served as the initial parameter fields for the DA experiments. Figure 3 shows the initial ensemble mean as well as one stochastic realization of the random K_{rb} and K_{aq} fields.

For the aquifer, 128 stochastic realizations of multi-Gaussian distributed random K_{aq} fields were generated with the sequential Gaussian simulation algorithm in SGeMS (Remy et al., 2009). The geostatistical variogram parameters used for generating the K_{aq} fields are listed in Table 1. A spherical variogram was selected, with a mean value of -2.53 $\log_{10}$ (m/s) and a sill value of 0.1 $\log_{10}$ (m^2/s^2). The semivariogram range was set to 150 m, which is approximately 10% of the horizontal model domain size and which was used in absence of better information on the range parameter. The sequential Gaussian simulations were conditioned to two K_{aq} values of -2.42 $\log_{10}$ (m/s) and -2.76 $\log_{10}$ (m/s), which are obtained from pumping tests (Würsten, 1991).

For the riverbed, random K_{rb} fields were generated in a similar way. Table 1 provides the corresponding geostatistical parameters for the variogram. A mean value of -4.55 $\log_{10}$ (m/s) was used to generate the random K_{rb} fields, which is approximately 2 magnitudes lower than the K_{aq} values. The semivariogram range was set to 150 m, and a sill value of 0.3 $\log_{10}$ (m^2/s^2) was used. The generation of the random K_{rb} fields was unconditional as no measurement data were available for the riverbed.

4. Numerical Experiments With EnKF-HGS

4.1. Overview

Simulation experiments were carried out using the numerical model described in section 3.2. DA was performed using measurement data from the year 2014, and measurements from the year 2015 were used as a verification data set. As the major flood event happened on 24 July 2014, for the simulations from 25 July 2014 onward two models with different riverbed topography were used: one model with the preflood riverbed topography and one with the postflood riverbed topography.

Multiple DA scenarios were tested: To systematically investigate the influence of riverbed topography on the inverse estimation of K_{rb} and K_{aq} as well as the prediction of hydraulic heads and exchange fluxes, the DA

Table 1
Variogram Parameters Used for Generating the K_{aq} and K_{rb} Fields

K	Type	Mean ($\log_{10}$ m/s)	Nugget	Range (m)	Sill ($\log_{10}$ m/s)
K_{aq}	Spherical	−2.53	0	150	0.1
K_{rb}	Spherical	−4.55	0	150	0.3

experiments were organized according to 10 different scenarios, divided into two groups. In the first group, changes in riverbed topography induced by the flood event were considered, whereas in the second group these changes were not considered. The different simulation experiments in both groups are described in detail in section 4.4.

4.2. Observation Data Set

Hydraulic heads within the model domain were measured at seven observation points (see Figure 1): A4, A7, A19, A24, A25, A26, and A35. The SW measurement station SW1 is located on top of a weir directly on the downstream model boundary and measures the SW discharge leaving the study site. Figure 4 displays the measured hydraulic heads and the SW discharge for the years 2014 and 2015. Measurements from A24, A25, and A26 are available for the entire 2-year simulation period, while for the locations A4, A7, A19, and A35 some gaps exist. The hydraulic head observations of the year 2014 are used for the DA experiments, and the hydraulic head observations of the year 2015 are used as a validation data set. For DA experiments, the measurement error was set to 5 cm for five of the measurement locations (A4, A7, A19, A25, and A35),

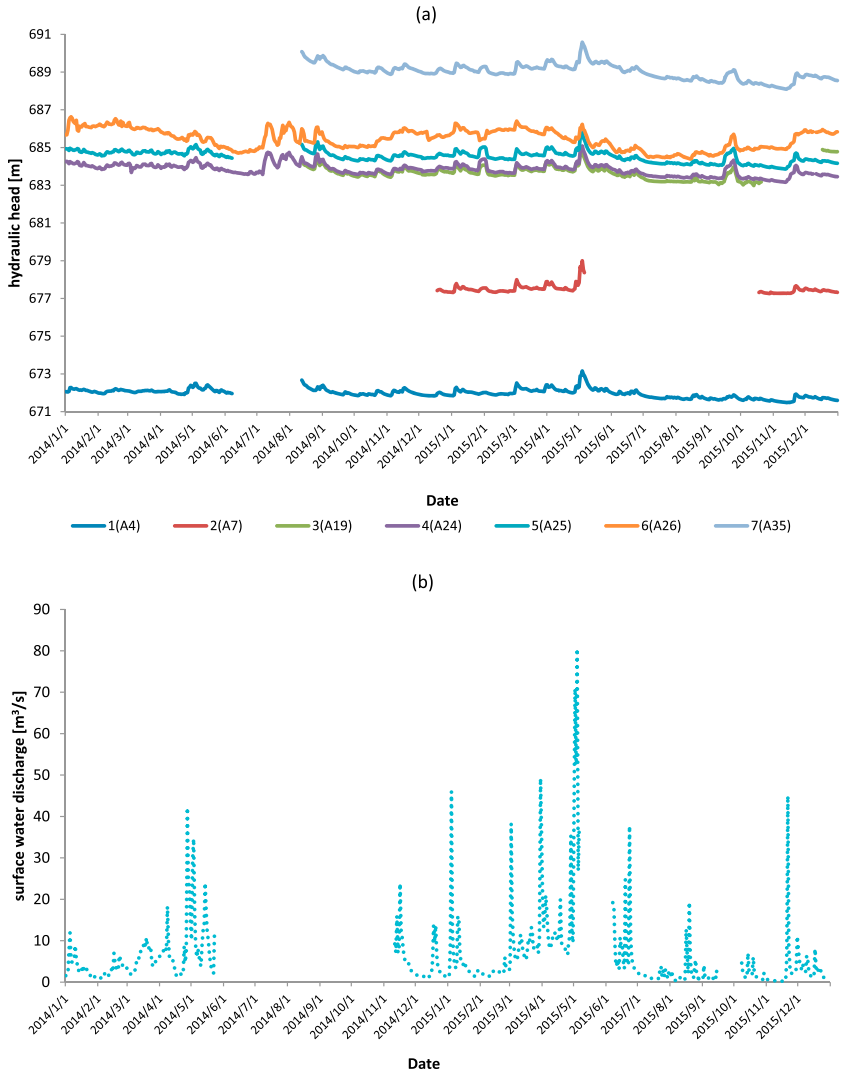

Figure 4. Measurements of (a) hydraulic head and (b) surface water discharge for the 2-year simulation period 2014 and 2015.

and 20 cm for two other locations (A24 and A26). Relatively high measurement errors were used for the latter two observation locations due to the fact that these piezometers are historic locations, which are not well serviced anymore. The SW discharge measurements of the year 2015 are also used to evaluate the model performance.

4.3. Model Spin-Up

Prior to the DA, spin-up simulations were carried out in order to obtain suitable initial conditions: In a first spin-up step, a steady state simulation with one randomly chosen realization of the stochastic *K* fields was run using boundary conditions corresponding to the annual average values of 2013. In a second spin-up step, individual exit-spin-up simulations for all 128 stochastic realizations of *K* fields were run for 20 days. Results from the steady state spin-up run were used as initial conditions for these exit-spin-up simulations, and transient boundary conditions of the first 20 days of January 2014 were imposed. The exit-spin-up runs produced an adequate initial ensemble spread adapted to the multiple stochastic *K* fields for the subsequent DA experiments.

4.4. Data Assimilation and Verification Experiments

DA experiments were carried out by assimilation of the hydraulic head observations, updating both the hydraulic heads and hydraulic conductivities. Due to the riverbed-changing flood event, the assimilation year 2014 was divided into two periods: a *preflood period* from 1 January 2014 until 24 July 2014, the day the flood occurred, and a *postflood period* from 25 July 2014 until 31 December 2014. As outlined in section 4.1, the DA scenarios were divided into two groups, the difference being whether UAV-based riverbed topography observations were incorporated or not. In Group 1 the preflood riverbed was used and the riverbed topography remained unchanged before and after the flood event (denoted by *_old*), while in Group 2 a new riverbed corresponding to the measured postflood topography was used for the postflood period (denoted by *_new*). As outlined in section 4.1, each of the two groups consisted of five different simulation scenarios. The differences between these scenarios were the assimilation of piezometric head data (yes or no), and the period during which these observations were assimilated (only before the flood, or also after the flood event). The different DA scenarios can be described as follows:

1. An OL scenario without assimilation and update, denoted by *OL*.
2. A scenario where hydraulic heads, K_{aq} and K_{rb}, were updated during the preflood period, but without update during the postflood period, denoted by *DA_OL*.
3. A scenario where hydraulic heads, K_{aq} and K_{rb}, were updated during the preflood period, but during the postflood period only hydraulic heads and K_{rb} were updated, denoted by *DA_hKr*.
4. A scenario with the same preflood updates as for scenarios 2 and 3 but where during the postflood period only hydraulic heads and K_{aq} were updated, denoted by *DA_hKa*.
5. A scenario where hydraulic heads, K_{aq} and K_{rb}, were updated both during the preflood period and the postflood period of the DA year 2014, denoted by *DA_hKrKa*.

An overview of all the simulation scenarios is provided in Table 2.

To eliminate any potential effects of initial conditions during the performance evaluation, pure verification experiments were carried out using measurements of the year 2015. For each of the different simulation scenarios, the same riverbed topography as used during the postflood period in 2014 was also used for the verification period. The simulated hydraulic heads and the calibrated *K* fields of the last time step of the assimilation period (i.e., end of 31 December 2014) were taken as initial conditions and parameter fields for the verification period. During the verification period, no DA or update of states or parameters was carried out.

For each of the simulation scenarios 128 stochastic realizations were used. Each realization used one processor, so that in total 128 processors in parallel were used. The 10 simulation scenarios, which were run over a period of 2 years, needed 430,080 core compute hours on the supercomputer JURECA (Krause & Thörnig, 2016) at Forschungszentrum Jülich.

4.5. Performance Measures

The root-mean-square error (RMSE) was used to evaluate the model performance by comparing simulated and measured hydraulic heads and SW discharge for the verification period. The RMSE for the simulated

Table 2
Simulation Scenarios With Different Riverbed Topography (RBT), Updating Variables, and for Different Time Periods

Simulation scenarios	Before flood (2014.1.1–2014.7.24)				After flood (2014.7.25–2014-12-31)				Verification year 2015
	RBT	Update h	Update K_{rb}	Update K_{aq}	RBT	Update h	Update K_{rb}	Update K_{aq}	RBT
OL_old	old	N	N	N	old	N	N	N	old
OL_new	old	N	N	N	new	N	N	N	new
DA_OL_old	old	Y	Y	Y	old	N	N	N	old
DA_OL_new	old	Y	Y	Y	new	N	N	N	new
DA_hKr_old	old	Y	Y	Y	old	Y	Y	N	old
DA_hKr_new	old	Y	Y	Y	new	Y	Y	N	new
DA_hKa_old	old	Y	Y	Y	old	Y	N	Y	old
DA_hKa_new	old	Y	Y	Y	new	Y	N	Y	new
DA_hKrKa_old	old	Y	Y	Y	old	Y	Y	Y	old
DA_hKrKa_new	old	Y	Y	Y	new	Y	Y	Y	new

hydraulic heads was calculated by comparing the ensemble mean value of the simulated heads to the measured hydraulic heads, averaged over all time steps and all observation locations:

$$\mathrm{RMSE}(h) = \sqrt{\frac{1}{n_t n_{\mathrm{nodes\_obs}}} \sum_{i=1}^{n_t} \sum_{j=1}^{n_{\mathrm{nodes\_obs}}} \left(\overline{h}_{i,j}^{f} - h_{i,j}^{\mathrm{obs}}\right)^2} \tag{12}$$

where h is the hydraulic head, n_t is the number of simulation time steps, $n_{\mathrm{nodes\_obs}}$ is the total number of the observation locations that differs for different simulation periods, the overbar indicates ensemble average, the superscript f indicates simulations, and the superscript obs is the observations. In our case, n_t equals 365 and $n_{\mathrm{nodes\_obs}}$ is 7.

The RMSE for the SW discharge is calculated by comparing the ensemble mean value of the simulated flow rate at the outlet with the measurement value, averaged over all time steps:

$$\mathrm{RMSE}(Q) = \sqrt{\frac{1}{n_t} \sum_{i=1}^{n_t} \left(\overline{Q}_i^{f} - Q_i^{\mathrm{obs}}\right)^2} \tag{13}$$

where Q is the SW discharge.

Temporal evolution of RMSE for the simulated hydraulic heads and SW discharge is also calculated by

$$\mathrm{RMSE}(h,t) = \sqrt{\frac{1}{n_{\mathrm{nodes\_obs}}} \sum_{j=1}^{n_{\mathrm{nodes\_obs}}} \left(\overline{h}_{j,t}^{f} - h_{j,t}^{\mathrm{obs}}\right)^2} \tag{14}$$

$$\mathrm{RMSE}(Q,t) = \left|\overline{Q}_t^{f} - Q_t^{obs}\right| \tag{15}$$

5. Results and Discussion

5.1. Reproduction of Heads

In Figure 5, hydraulic head maps for scenario OL_old and DA_hKrKa_new are provided as examples. Shown is the first day of the verification year 2015.

In Figure 6 examples of simulated against observed hydraulic heads are provided for the OL scenario OL_old and the DA scenario DA_hKrKa_new for the verification year 2015 at observation location A4. The plots show that at this observation location the OL simulations are associated with a bias, which is removed in the DA scenario where both K_{rb} and K_{aq} are updated.

To evaluate the performance of simulated heads over all observation locations, the scores of the RMSE(h) for different simulation scenarios are provided in Table 3. In the verification period, the RMSE(h) for the OL simulation with the preflood riverbed topography (scenario OL_old) is 0.766 m and with the

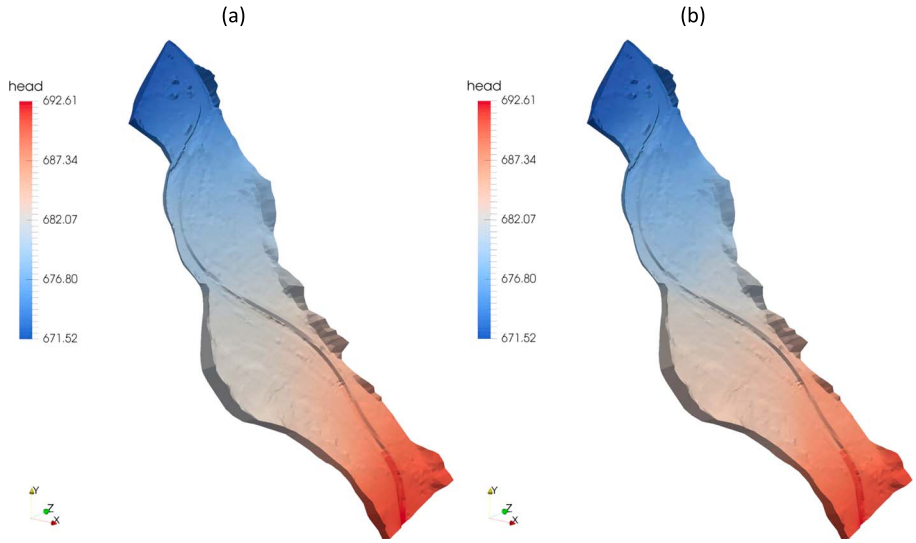

Figure 5. Groundwater head maps for scenario (a) OL_old and (b) DA_hKrKa_new for the first day of the verification year 2015.

postflood riverbed topography (scenario OL_new) 0.579 m. The RMSE(*h*) was therefore reduced by 24% through the incorporation of the post flood riverbed topography. This indicates that adapting the riverbed topography after the flood event has a positive influence on the estimation of hydraulic heads and that the UAV-based observation and subsequent implementation of the postflood riverbed topography in the hydrological flow model lead to a better reproduction of hydraulic heads, if no calibration of the parameter fields is made.

If in the verification period the preflood riverbed topography is used, and if hydraulic heads, K_{aq} and K_{rb}, were only updated in the preflood period (scenario DA_OL_old) the RMSE(*h*) is 0.659 m, which is 13.4% lower than its OL counterpart (scenario OL_old). This demonstrates that DA can improve the simulation of hydraulic heads through parameter updating. However, the improvement is less compared to the equivalent scenario, which used the postflood riverbed topography (scenario OL_new). This again indicates that the implementation of UAV-based observations of riverbed topography modification improves the simulation of river-aquifer systems.

If, for the model with the preflood riverbed topography, states and parameters are also updated in the postflood period (scenario DA_hKrKa_old), the RMSE(*h*) is reduced by 51.7% (RMSE [*h*] = 0.370 m) compared to the OL with the preflood riverbed topography. Interestingly, this is only slightly less performant

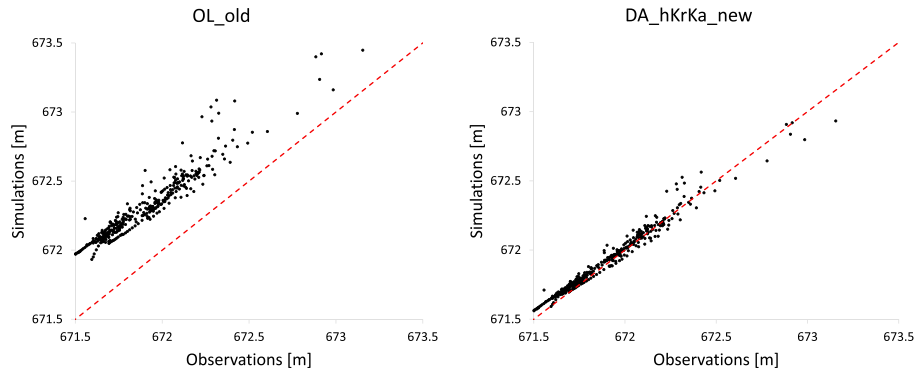

Figure 6. 1:1 Plot of simulated versus observed hydraulic heads for the open loop scenario OL_old and the DA scenario DA_hKrKa_new. Results are shown for the observation point A4 and the year 2015.

Table 3
RMSE of Simulated Heads and Surface Water Discharge for Different Simulation Scenarios for the Verification Period

Simulation scenarios	RMSE (h) (m)	RMSE (Q) (m^3/s)
OL_old	0.766	4.17
OL_new	0.579	4.15
DA_OL_old	0.659	4.14
DA_OL_new	0.581	4.11
DA_hKr_old	0.449	4.06
DA_hKr_new	0.630	4.13
DA_hKa_old	0.513	4.09
DA_hKa_new	0.357	4.23
DA_hKrKa_old	0.370	4.04
DA_hKrKa_new	0.348	4.18

than the equivalent scenario but using the postflood riverbed topography (scenario DA_hKrKa_new) (RMSE [h] = 0.348 m). This result suggests that if a major flood event changes the riverbed topography, but no direct observations of these changes are available, DA of hydraulic heads, in which both states as well as K_{rb} and K_{aq} are simultaneously updated, can mostly compensate for the missing riverbed topography observations, at least in terms of the reproduction of hydraulic heads. If riverbed topography changes are not accounted for, a quite similar impact on the hydraulic heads can be simulated by changing K_{rb} and/or K_{aq}. For example, in case of sedimentation processes, which are not accounted for, a quite similar impact on hydraulic heads can be obtained by decreasing K_{rb} and possibly also the model layers below.

If the postflood riverbed topography is used after the flood, but hydraulic heads as well as K_{aq} and K_{rb} are only updated in the preflood period (scenario DA_OL_new), the RMSE (h) is 0.581 m. This performance is similar to the OL counterpart (scenario OL_new) (RMSE [h] = 0.579 m). This poor performance is probably due to the fact that the K_{rb} fields are

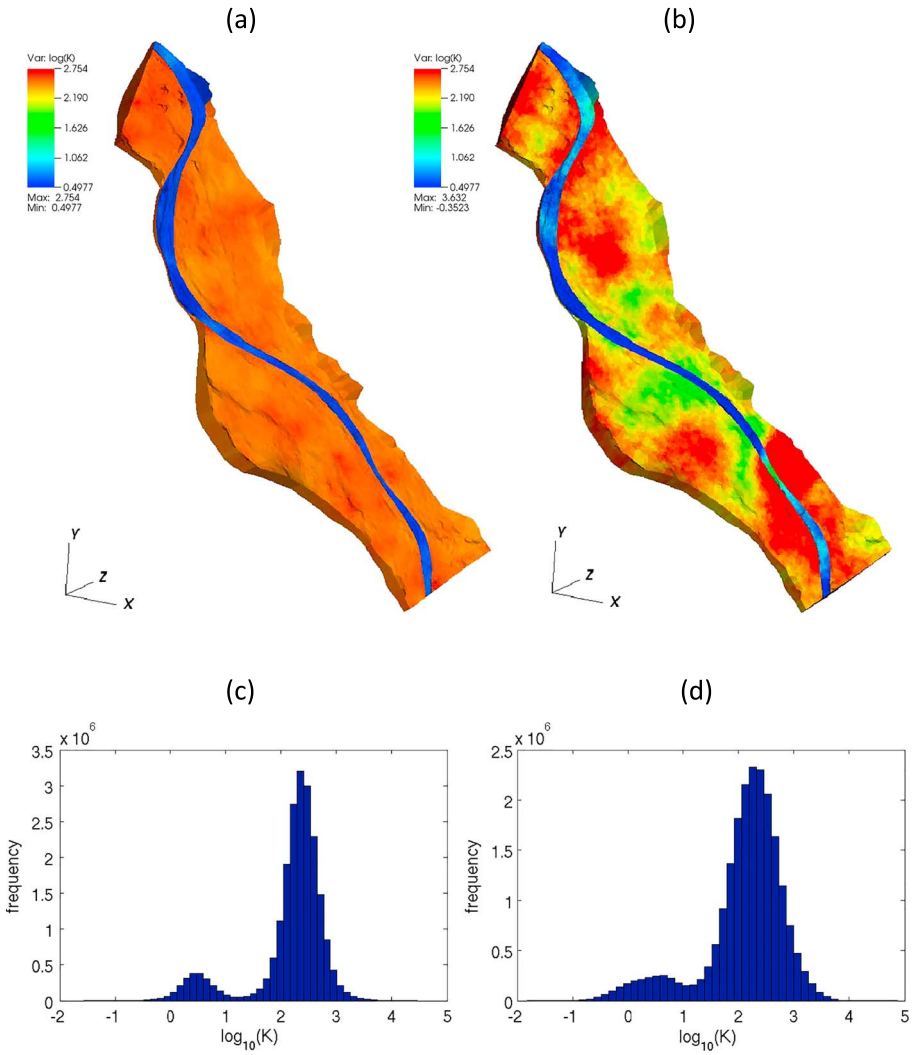

Figure 7. The ensemble mean of K_{aq} and K_{rb} Fields (a) for all simulation scenarios at the initial time step (t = 01.01.2014) and (b) for scenarios where data assimilation is done in the preflood period at the final time step of the preflood period (t = 24.07.2014) after data assimilation. (c and d) Corresponding histograms are provided. (Unit: m/day).

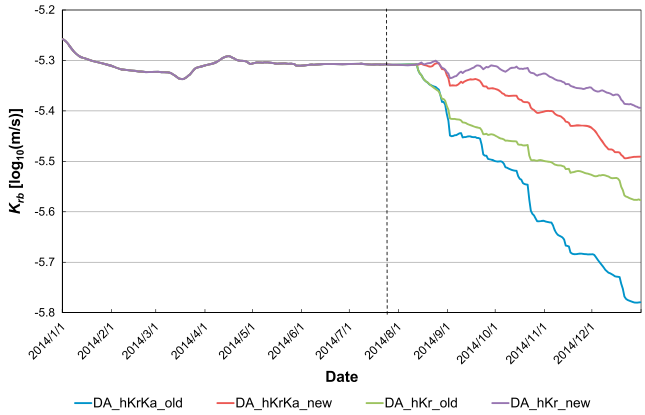

Figure 8. Temporal evolution of average K_{rb} for different simulation scenarios for the assimilation year 2014. Shown are four scenarios where different variables are updated in the postflood period: scenario with update of heads, K_{rb} and K_{aq}, using the old riverbed topography (blue line, DA_hKrKa_old); scenario with update of heads, K_{rb} and K_{aq}, using the new riverbed topography (red line, DA_hKrKa_new); scenario with update of heads and K_{rb} using the old riverbed topography (green line, DA_hKr_old); and scenario with update of heads and K_{rb} using the new riverbed topography (purple line, DA_hKr_new). The flood event was marked in dash, black line.

estimated based on the preflood riverbed topography, which is not in correspondence with the postflood riverbed topography. Nevertheless, the RMSE (h) is still 11.6% lower than the scenario where the riverbed topography was not updated after the flood (scenario DA_OL_old). This again highlights the benefit of updating riverbed topography for the estimation of hydraulic heads.

If all available information is used and all states and parameters are updated, that is, if the postflood riverbed topography is used and hydraulic heads, K_{rb} and K_{aq} are updated after the flood (scenario DA_hKrKa_new), the RMSE(h) is reduced to 0.348 m. Unsurprisingly, this scenario performs best among all the scenarios. It is 39.9% lower than the equivalent OL run OL_new and 40.1% lower than the scenario with updating only during the preflood period. The reduction is less when compared to the scenario with the preflood riverbed topography (scenario DA_hKrKa_old, reduction 51.7%), because the postflood riverbed topography already provides important information on the riverbed, and estimation of the K field is therefore less important than for the scenario where no information on the postflood riverbed topography is available.

That information on riverbed topography is important that can be further seen by comparing scenarios where both K_{aq} and K_{rb} are updated to scenarios where only one of the two K fields is updated. Updating both K fields corresponds to scenarios DA_hKrKa_old and DA_hKrKa_new, while updating only one of the two K fields to scenarios DA_hKr_old, DA_hKr_new, DA_hKa_old, and DA_hKa_new. Comparison of RMSE (h) reveals that both for the preflood or postflood riverbed topography, updating only K_{aq} or only K_{rb} results in a poorer performance than updating both. With the preflood topography, the RMSE (h) for the scenario with update of only K_{rb} is 0.449 m, and with update of only K_{aq} 0.513 m. These values are 21.3% and 38.6% higher than the scenario with update of both K_{aq} and K_{rb} (RMSE [h] = 0.370 m).

The updating of K_{rb} and riverbed topography after the flood event resulted in a better characterization of hydraulic heads in the verification period for all simulation scenarios except for one: Updating of K_{aq} in the postflood period resulted in improved RMSE (h) of 0.357 m for the scenario where only K_{aq} was updated, and in 0.348 m where K_{aq} was updated together with K_{rb}. However, when the postflood riverbed topography was used for the postflood period, the RMSE (h) for the scenario where only K_{rb} was updated was 0.63 m (DA_hKr_new), which is slightly worse compared to the scenarios where only the riverbed topography was updated in the postflood period (OL_new and DA_OL_new). The poor performance of DA_hKr_new suggests that major flood events such as the one studied not only have a strong impact on the riverbed but even on the underlying aquifer sediments. Therefore, when topographic changes are taken into account in the flow simulations, resulting in considerable changes in topography, which are so large that locally the complete former riverbed is removed, optimal reproduction of postflood hydraulic heads requires not only K_{rb} to be updated but also K_{aq}. The importance of updating K_{aq} in the postflood period, if the observed, riverbed topography information is considered, can be again proved by comparing with scenario DA_hKa_new (RMSE [h] = 0.357 m) where only K_{aq} is updated and scenario DA_hKrKa_new (RMSE [h] = 0.348 m) where K_{aq} is updated together with K_{rb}. Nevertheless, in case of a lack of information on riverbed topography modification and if K_{aq} has been estimated reasonably well prior to a major flood event, updating K_{rb} after the flood event is more important than continuing to update K_{aq}. Moreover, the results indicate that this DA strategy can partly compensate for a lack of information on flood event induced changes to the riverbed topography. The results do, however, show that updating of K_{aq} is a first-order control for the reproduction of hydraulic heads and that a good estimation of K_{aq} coupled with the incorporation of observations of riverbed topography changes into the flow model might be more performant than only updating of K_{rb} and riverbed topography alone. In other words, a good estimation of aquifer properties cannot be compensated by observations and estimations of riverbed properties alone.

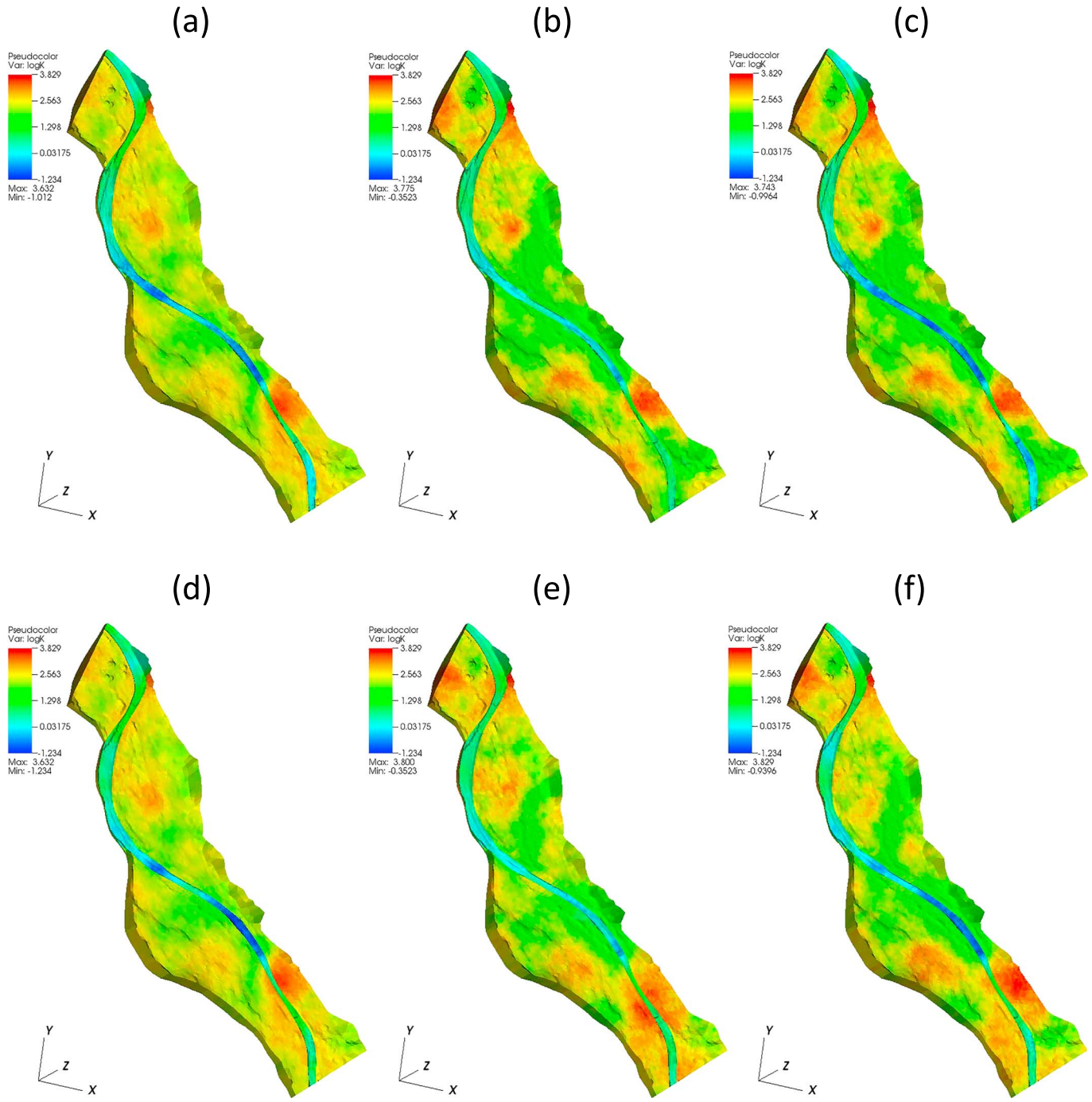

Figure 9. The final updated K fields at the end of the postflood period (t = 2014.12.31) for different simulation scenarios: (a) scenario DA_hKr_old, (b) scenario DA_hKa_old, (c) scenario DA_hKrKa_old, (d) scenario DA_hKr_new, (e) scenario DA_hKa_new, and (f) scenario DA_hKrKa_new. Scenarios using the pre-flood topography are displayed in the upper row, while scenarios using the postflood topography are displayed in the bottom row.

5.2. Evolution of K_{aq} and K_{rb}

Figure 7 shows the ensemble mean K_{aq} and K_{rb} fields at the initial (t = 01.01.2014) and the final time step (t = 24.07.2014) of the preflood period. The initial fields are the same for all simulation scenarios, and the shown final fields are only for scenarios with DA in the preflood period. The $\log_{10}$ (K_{aq}) values are between −5.29 and −1.30 $\log_{10}$ (m/s) for the final updated field and between −4.44 and −2.19 $\log_{10}$ (m/s) for the

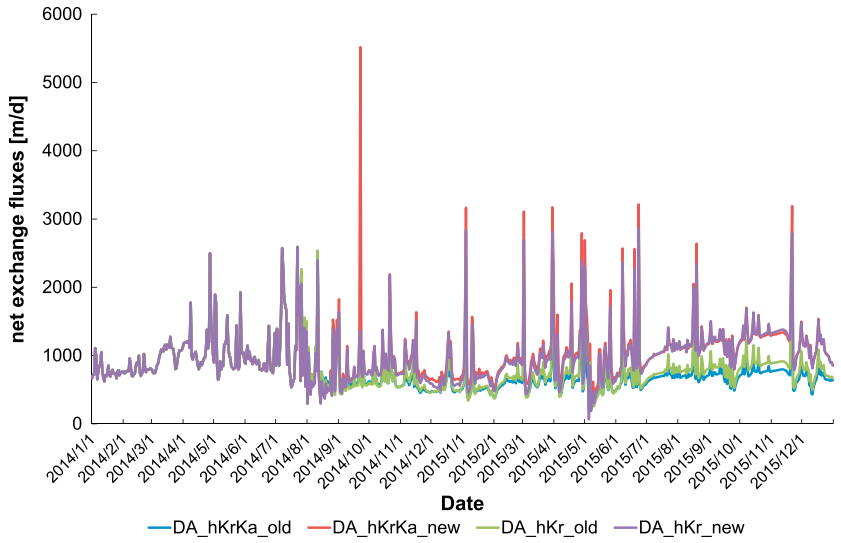

Figure 10. Temporal evolution of net exchange fluxes between the surface and subsurface domain. Shown is the mean value calculated over 128 realizations. Positive values indicate infiltration from the surface water into the subsurface.

initial field. The final updated ensemble mean K_{aq} and K_{rb} fields show a larger spatial variability than the prior ensemble mean fields. As no measurement data are available for K_{rb}, and the only two K_{aq} measurements are used for generating the initial K_{aq} and K_{rb} fields, it is not possible to directly evaluate if the updated K_{aq} and K_{rb} fields are closer to the true values. However, these updated K_{aq} and K_{rb} fields improved the characterization of heads by 29% in the preflood period.

The temporal evolution of K_{rb} averaged over all the riverbed elements is displayed for different simulation scenarios in Figure 8. In the preflood period these four scenarios are exactly the same, and the following results focus on the postflood period: The estimated K_{rb} in the postflood period is lower for scenarios with the preflood riverbed topography than for the scenarios with the postflood one, which highlights the fact that the K_{rb} does not need to be altered that much for a good reproduction of hydraulic heads if the riverbed topography is also updated. Moreover, whether the old or the new riverbed topography is used, the reduction of K_{rb} through DA is larger for scenarios where both K_{aq} and K_{rb} are updated than for scenarios where only K_{rb} is updated.

Figure 9 shows the ensemble mean K_{aq} and K_{rb} fields at the end of the postflood period (t = 31.12.2014) for scenarios with DA also during the postflood period. Scenarios with the postflood riverbed topography show slightly higher and smoother K_{aq} and K_{rb} values than scenarios with the preflood riverbed topography, which is also consistent with the analysis above and the head results in section 5.1.

5.3. Simulation of Exchange Fluxes and Surface Water Discharge (Q)

Figure 10 displays the temporal evolution of exchange fluxes between surface and sub-SW. In the preflood period all plotted scenarios give the same results as there are no differences between the simulations. Differences among the scenarios are minor in the postflood period but become larger in the second half of 2015. Differences are particularly large between scenarios with the preflood and scenarios with the postflood riverbed topography, which is consistent with the reduction of K_{rb} (see Figure 6). The lower the K_{rb} is, the less infiltration is observed.

Hydrographs showing simulated versus observed river discharge are provided in Figure 11 for the OL scenario OL_old and the DA scenario DA_hKrKa_new. The largest mismatch between simulated and observed peaks is 40 m^3/s during the extreme peak flood. The performance of the different simulation scenarios in terms of the reproduction of SW discharge is summarized in Table 3. The difference of RMSE(Q) between the two OL runs with different riverbed topographies is 0.02 m^3/day. This indicates that an update of the riverbed topography also slightly improves the representation of SW discharge,

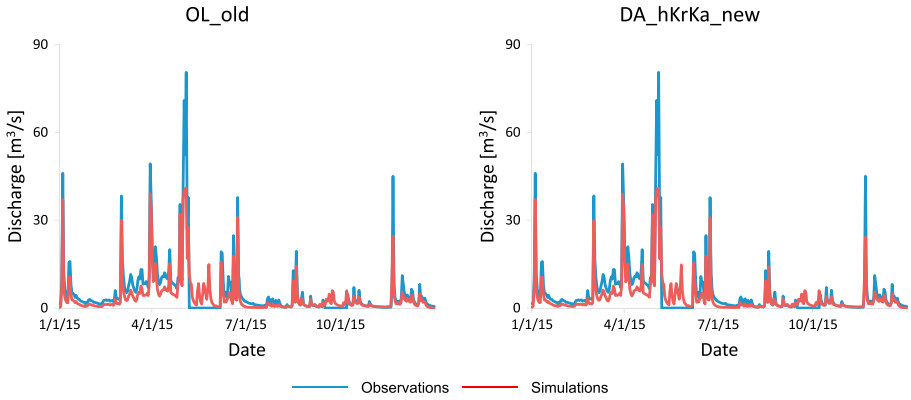

Figure 11. Hydrographs of simulated versus observed river discharge for the scenarios OL_old and DA_hKrKa_new.

but the impact is very small. If the preflood riverbed topography is used and hydraulic heads, K_{aq} and K_{rb} are updated only in the preflood period (scenario DA_OL_old), the RMSE(Q) is 4.14 m^3/day, which is only 0.03 m^3/day lower than for the OL counterpart OL_old. However, if all of these variables are continuously updated by EnKF in the postflood period (scenario DA_hKrKa_old), the RMSE(Q) decreases to 4.04 m^3/day. This shows that without information on the postflood riverbed topography, DA based on EnKF can nonetheless improve the characterization of SW discharge via updating of parameters and hydraulic heads. Altogether, scenarios where both K_{aq} and K_{rb} are updated (scenario DA_hKrKa_old) resulted in the smallest RMSE(Q). This is consistent with the results for hydraulic heads discussed in section 5.1.

On the other hand, if the postflood riverbed topography is included in the simulations, the RMSE(Q) for the scenario where hydraulic heads, K_{aq} and K_{rb}, are updated in the preflood period (scenario DA_OL_new) is 0.04 m^3/day lower than for the OL counterpart (scenario OL_new). However, DA in the postflood period did not improve SW discharge characterization but deteriorated it in most cases results. Only the scenario with update of K_{rb} (scenario DA_hKr_new) provided slightly better results than the corresponding OL run (scenario OL_new). The temporal evolution of simulated SW discharge against the measurement (not displayed) also indicates that differences between the different simulation scenarios are small, and differences with the measurements are mostly small except for periods with large discharge rates, for example, in May 2015. Altogether, updating riverbed topography and updating K_{rb} improve SW discharge estimation, but if riverbed topography and K_{rb} are already updated, the additional updating of K_{aq} deteriorates results instead of improving them. This illustrates that updating the riverbed topography and K_{rb} has a small impact on the SW discharge, although the impact on the simulation of hydraulic heads and exchange fluxes is strong. This is mainly because the total exchange flux is much smaller than the total amount of the SW discharge.

6. Conclusions

In this study, we investigated the spatial and temporal variation of the K_{rb} and topography of the Emme river in Switzerland, induced by a 300-year flood event, with a combination of state-of-the-art UAV-based observations, integrated hydrological flow simulations and DA. We investigated the influence of the spatial and temporal changes in the riverbed topography and riverbed properties induced by the flood event on the simulation of hydraulic heads, SW discharge, and river-aquifer exchange fluxes using the physically based, fully integrated hydrological flow model HGS. Both riverbed topography data from before and after the flood event were used as input for the hydrological flow model. DA experiments were performed with the EnKF for the preflood and postflood periods, either under consideration of the changes of riverbed topography, or while ignoring them. Heterogeneous multi-Gaussian distributed K_{aq} and K_{rb} fields were used as the initial parameter fields and later, together with hydraulic heads, updated by EnKF. Verification experiments of the postflood year (2015) were used for evaluating the performance

of the different parameter/states/topography updating schemes. The following conclusions can be drawn from our experiments:

1. Changes in riverbed topography have a significant influence on the prediction of hydraulic heads and river-aquifer exchange fluxes and a minor influence on the prediction of SW discharge. Incorporation of information on the modified riverbed topography obtained via unmanned-aerial-vehicle-based through-water photogrammetry improves the simulation of hydraulic heads.
2. The estimation of K_{aq} and K_{rb} with help of DA allows a better estimation of hydraulic heads and a slightly better estimation of SW discharge, even if DA is only carried out before the flood event. The parameter estimation is especially important, if changes in riverbed topography are not taken into account in the postflood simulations, because it allows compensating for this lack of information.
3. Both observations of the changes in riverbed topography and of hydraulic heads provide useful information for the simulation of river-aquifer systems. Without the riverbed topography information, estimation of both K_{rb} and K_{aq} is important. However, if K_{aq} could be estimated reasonably well prior to a flood event, and information on the transient changes of riverbed topography are available, a reestimation of K_{rb} seems to be less important.

With this study we could demonstrate that the combination of the state-of-the-art techniques of unmanned-aerial-vehicle-based remote sensing, physically based and fully integrated hydrological modeling with HGS, and EnKF-based DA allows substantially improving predictions of hydrological states and fluxes of river-aquifer systems. To the authors' knowledge, this is the first time these techniques were applied in an integrated way to a real-world system, and the combination of these techniques provides a promising new and affordable tool for the prediction of river-aquifer systems. Integrating of more data and other data types is expected to further improve the modeling of river-aquifer systems. These data could include observations of river discharge, soil moisture, and tracer concentrations in the river or near the river which provide (indirect) information on riverbed properties and temperatures in the river, riverbed, and GW. Until now, only very few studies used such diverse observations for DA when modeling river-aquifer interactions (e.g., Kurtz et al., 2014), and the most commonly used data types are river discharge and hydraulic heads (Bailey & Baù, 2010, 2012; Camporese et al., 2009; Pasetto et al., 2012). These papers (except Kurtz et al., 2014) however did not focus specifically on the riverbed and did not update riverbed hydraulic properties.

The practical application of these methods by hydrologic practitioners and water resource managers is possible with help of a small computer cluster, as only forecasts need to be calculated for the next day(s) on an operation level, for example, in the context of well-field management or flood forecasting. This was already shown by Hendricks Franssen et al. (2011). However, parameter estimation with help of historical information requires much larger amounts of compute time and for this cloud computing is an interesting option. Kurtz et al. (2017) already demonstrated the feasibility of a combination of near real-time physically based hydrological modeling, DA and near real-time control in a cloud computing environment. With the now widely available access to cloud computing resources, we feel that the application of these stochastic methods in practice is more hampered by the necessary understanding of stochastic methods and the preparation of large amounts of input information (e.g., random fields) than by the needed computing infrastructure.

Acknowledgments
The authors gratefully acknowledge the computing time granted by the JARA-HPC Vergabegremium and VSR commission on the supercomputer JURECA (Krause & Thörnig, 2016) at Forschungszentrum Jülich. The first author, Qi Tang, also acknowledges the financial support from China Scholarship Council (CSC). W. Kurtz gratefully acknowledges the funding provided by the German Research Foundation (DFG) for project SFB-TR32 "Patterns in soil-vegetation-atmosphere systems: monitoring, modeling and data assimilation." O. S. Schilling is grateful for the funding by the Swiss National Science Foundation grant P2NEP2_171985. All model input data used to reproduce the simulation results shown in the manuscript are provided in the supporting information data sets.

References

Ala-aho, P., Soulsby, C., Wang, H. L., & Tetzlaff, D. (2017). Integrated surface-subsurface model to investigate the role of groundwater in headwater catchment runoff generation: A minimalist approach to parameterisation. *Journal of Hydrology*, *547*, 664–677. https://doi.org/10.1016/j.jhydrol.2017.02.023

Alzraiee, A. H., Bailey, R., & Bau, D. (2017). Assimilation of historical head data to estimate spatial distributions of stream bed and aquifer hydraulic conductivity fields. *Hydrological Processes*, *31*(7), 1527–1538. https://doi.org/10.1002/hyp.11123

Ameli, A. A., & Creed, I. F. (2017). Quantifying hydrologic connectivity of wetlands to surface water systems. *Hydrology and Earth System Sciences*, *21*(3), 1791–1808. https://doi.org/10.5194/hess-21-1791-2017

Anderson, M. P., Woessner, W. W., & Hunt, R. J. (2015). *Applied groundwater modeling: simulation of flow and advective transport*. San Diego, CA: Academic Press.

Aquanty Inc. (2016). HydroGeoSphere. A three-dimensional numerical model describing fully integrated subsurface and surface flow and solute transport. *Waterloo, ON, Canada*.

Bailey, R. T., & Baù, D. (2010). Ensemble smoother assimilation of hydraulic head and return flow data to estimate hydraulic conductivity distribution. *Water Resources Research*, *46*, W12543. https://doi.org/10.1029/2010WR009147

Bailey, R. T., & Baù, D. (2012). Estimating geostatistical parameters and spatially-variable hydraulic conductivity within a catchment system using an ensemble smoother. *Hydrology and Earth System Sciences*, *16*(2), 287–304. https://doi.org/10.5194/hess-16-287-2012

Banks, E., Brunner, P., & Simmons, C. T. (2011). Vegetation controls on variably saturated processes between surface water and groundwater and their impact on the state of connection. *Water Resources Research*, *47*, W11517. https://doi.org/10.1029/2011WR010544

Birck, M. D. (2006). Temporal variability of riverbed hydraulic conductivity at an induced infiltration site, southwest Ohio. Miami University.

Blau, R. V., & Muchenberger, F. (1997). Grundlagen für Schutz und Bewirtschaftung der Grundwasser des Kantons Bern: Nutzungs-, Schutz- und Überwachungskonzept für die Grundwasserleiter des obersten Emmentals, zwischen Emmenmatt, Langnau und Eggiwil, Synthesebericht, Wasser- und Energiewirtschaft des Kantons Bern, Bern.

Blessent, D., Therrien, R., & Gable, C. W. (2011). Large-scale numerical simulation of groundwater flow and solute transport in discretely-fractured crystalline bedrock. *Advances in Water Resources*, *34*(12), 1539–1552. https://doi.org/10.1016/j.advwatres.2011.09.008

Boano, F., Demaria, A., Revelli, R., & Ridolfi, L. (2010). Biogeochemical zonation due to intrameander hyporheic flow. *Water Resources Research*, *46*, W07535. https://doi.org/10.1029/2008WR007583

Brunner, P., Doherty, J., & Simmons, C. T. (2012). Uncertainty assessment and implications for data acquisition in support of integrated hydrologic models. *Water Resources Research*, *48*, W07513. https://doi.org/10.1029/2011WR011342

Brunner, P., & Simmons, C. T. (2012). HydroGeoSphere: A fully integrated, physically based hydrological model. *Ground Water*, *50*(2), 170–176.

Brunner, P., Therrien, R., Renard, P., Simmons, C. T., & Hendricks Franssen, H. J. (2017). Advances in understanding river-groundwater interactions. *Reviews of Geophysics*, *55*, 818–854. https://doi.org/10.1002/2017RG000556

Camporese, M., Paniconi, C., Putti, M., & Salandin, P. (2009). Ensemble Kalman filter data assimilation for a process-based catchment scale model of surface and subsurface flow. *Water Resources Research*, *45*, W10421. https://doi.org/10.1029/2008WR007031

Cardenas, M. B. (2009). Stream-aquifer interactions and hyporheic exchange in gaining and losing sinuous streams. *Water Resources Research*, *45*, W06429. https://doi.org/10.1029/2008WR007651

Cardenas, M. B., Wilson, J., & Zlotnik, V. A. (2004). Impact of heterogeneity, bed forms, and stream curvature on subchannel hyporheic exchange. *Water Resources Research*, *40*, W08307. https://doi.org/10.1029/2004WR003008

Chen, Y., & Zhang, D. (2006). Data assimilation for transient flow in geologic formations via ensemble Kalman filter. *Advances in Water Resources*, *29*(8), 1107–1122. https://doi.org/10.1016/j.advwatres.2005.09.007

Cornelissen, T., Diekkrüger, B., & Bogena, H. R. (2016). Using high-resolution data to test parameter sensitivity of the distributed hydrological model HydroGeoSphere. *Water*, *8*(5), 202. https://doi.org/10.3390/w8050202

de Rooij, R. (2017). New insights into the differences between the dual node approach and the common node approach for coupling surface–subsurface flow. *Hydrology and Earth System Sciences*, *21*(11), 5709–5724. https://doi.org/10.5194/hess-21-5709-2017

Doherty, J. (2015). *Calibration and uncertainty analysis for complex environmental models.–PEST: Complete theory and what it means for modelling the real world*. Brisbane, Australia: Watermark Numerical Computing.

Doppler, T., Franssen, H.-J. H., Kaiser, H.-P., Kuhlman, U., & Stauffer, F. (2007). Field evidence of a dynamic leakage coefficient for modelling river–aquifer interactions. *Journal of Hydrology*, *347*(1-2), 177–187. https://doi.org/10.1016/j.jhydrol.2007.09.017

Evensen, G. (1994). Sequential data assimilation with a nonlinear quasi-geostrophic model using Monte Carlo methods to forecast error statistics. *Journal of Geophysical Research*, *99*(C5), 10143–10,162. https://doi.org/10.1029/94JC00572

Fetter, C. W. (2000). *Applied hydrogeology*. Upper Saddle River, NJ: Prentice Hall.

Feurer, D., Bailly, J.-S., Puech, C., Le Coarer, Y., & Viau, A. A. (2008). Very-high-resolution mapping of river-immersed topography by remote sensing. *Progress in Physical Geography*, *32*(4), 403–419. https://doi.org/10.1177/0309133308096030

Figura, S., Livingstone, D. M., & Kipfer, R. (2013). Competing controls on groundwater oxygen concentrations revealed in multidecadal time series from riverbank filtration sites. *Water Resources Research*, *49*, 7411–7426. https://doi.org/10.1002/2013WR013750

Figura, S., Livingstone, D. M., & Kipfer, R. (2015). Forecasting groundwater temperature with linear regression models using historical data. *Groundwater*, *53*(6), 943–954. https://doi.org/10.1111/gwat.12289

Frei, S., Lischeid, G., & Fleckenstein, J. (2010). Effects of micro-topography on surface–subsurface exchange and runoff generation in a virtual riparian wetland—A modeling study. *Advances in Water Resources*, *33*(11), 1388–1401. https://doi.org/10.1016/j.advwatres.2010.07.006

Gianni, G., Richon, J., Perrochet, P., Vogel, A., & Brunner, P. (2016). Rapid identification of transience in streambed conductance by inversion of floodwave responses. *Water Resources Research*, *52*, 2647–2658. https://doi.org/10.1002/2015WR017154

Grischek, T., & Bartak, R. (2016). Riverbed clogging and sustainability of riverbank filtration. *Water*, *8*(12), 604. https://doi.org/10.3390/w8120604

Harvey, J. W., & Bencala, K. E. (1993). The effect of streambed topography on surface-subsurface water exchange in mountain catchments. *Water Resources Research*, *29*(1), 89–98. https://doi.org/10.1029/92WR01960

Harvey, J. W., Drummond, J. D., Martin, R. L., McPhillips, L. E., Packman, A. I., Jerolmack, D. J., et al. (2012). Hydrogeomorphology of the hyporheic zone: Stream solute and fine particle interactions with a dynamic streambed. *Journal of Geophysical Research*, *117*, G00N11. https://doi.org/10.1029/2012JG002043

Hendricks Franssen, H., Kaiser, H., Kuhlmann, U., Bauser, G., Stauffer, F., Müller, R., & Kinzelbach, W. (2011). Operational real-time modeling with ensemble Kalman filter of variably saturated subsurface flow including stream-aquifer interaction and parameter updating. *Water Resources Research*, *47*, W02532. https://doi.org/10.1029/2010WR009480

Hendricks Franssen, H., & Kinzelbach, W. (2008). Real-time groundwater flow modeling with the ensemble Kalman filter: Joint estimation of states and parameters and the filter inbreeding problem. *Water Resources Research*, *44*, W09408. https://doi.org/10.1029/2007WR006505

Hester, E. T., & Doyle, M. W. (2008). In-stream geomorphic structures as drivers of hyporheic exchange. *Water Resources Research*, *44*, W03417. https://doi.org/10.1029/2006WR005810

Hsieh, P. A., Wingle, W., & Healy, R. W. (2000). VS2DI—A graphical software package for simulating fluid flow and solute or energy transport in variably saturated porous media. *US Geological Survey Water-Resources Investigations Report*, *99*(4130), 16.

Irvine, D. J., Brunner, P., Franssen, H.-J. H., & Simmons, C. T. (2012). Heterogeneous or homogeneous? Implications of simplifying heterogeneous streambeds in models of losing streams. *Journal of Hydrology*, *424*, 16–23.

Kalbus, E., Schmidt, C., Molson, J., Reinstorf, F., & Schirmer, M. (2009). Influence of aquifer and streambed heterogeneity on the distribution of groundwater discharge. *Hydrology and Earth System Sciences*, *13*(1), 69–77. https://doi.org/10.5194/hess-13-69-2009

Karan, S., Engesgaard, P., & Rasmussen, J. (2014). Dynamic streambed fluxes during rainfall-runoff events. *Water Resources Research*, *50*, 2293–2311. https://doi.org/10.1002/2013WR014155

Kasahara, T., & Wondzell, S. M. (2003). Geomorphic controls on hyporheic exchange flow in mountain streams. *Water Resources Research*, *39*(1), 1005. https://doi.org/10.1029/2002WR001386

Käser, D. H., Binley, A., Heathwaite, A. L., & Krause, S. (2009). Spatio-temporal variations of hyporheic flow in a riffle-step-pool sequence. *Hydrological Processes*, *23*(15), 2138–2149. https://doi.org/10.1002/hyp.7317

Käser, D. H., & Hunkeler, D. (2016). Contribution of alluvial groundwater to the outflow of mountainous catchments. *Water Resources Research*, *52*, 680–697. https://doi.org/10.1002/2014WR016730

Krause, D., & Thörnig, P. (2016). JURECA: General-purpose supercomputer at Jülich Supercomputing Centre. *Journal of large-scale research facilities JLSRF*, *2*, 62.

Kropf, P., Schiller, E., Brunner, P., Schilling, O., Hunkeler, D., & Lapin, A. (2014). Wireless mesh networks and cloud computing for real time environmental simulations. In *Recent advances in information and communication technology* (pp. 1–11). New York: Springer.

Kurtz, W., Hendricks Franssen, H.-J., Brunner, P., & Vereecken, H. (2013). Is high-resolution inverse characterization of heterogeneous river bed hydraulic conductivities needed and possible? *Hydrology and Earth System Sciences*, *17*(10), 3795–3813. https://doi.org/10.5194/hess-17-3795-2013

Kurtz, W., Hendricks Franssen, H. J., Kaiser, H. P., & Vereecken, H. (2014). Joint assimilation of piezometric heads and groundwater temperatures for improved modeling of river-aquifer interactions. *Water Resources Research*, *50*, 1665–1688. https://doi.org/10.1002/2013wr014823

Kurtz, W., Hendricks Franssen, H. J., & Vereecken, H. (2012). Identification of time-variant river bed properties with the ensemble Kalman filter. *Water Resources Research*, *48*, W10534. https://doi.org/10.1029/2011WR011743

Kurtz, W., Lapin, A., Schilling, O. S., Tang, Q., Schiller, E., Braun, T., et al. (2017). Integrating hydrological modelling, data assimilation and cloud computing for real-time management of water resources. *Environmental Modelling & Software*, *93*, 418–435. http://doi.org/10.1016/j.envsoft.2017.03.011

Lackey, G., Neupauer, R. M., & Pitlick, J. (2015). Effects of streambed conductance on stream depletion. *Water*, *7*(12), 271–287. https://doi.org/10.3390/w7010271

Lapin, A., Schiller, E., Kropf, P., Schilling, O., Brunner, P., Kapic, A. J., et al. (2014). Real-time environmental monitoring for cloud-based hydrogeological modeling with hydrogeosphere. Paper presented at the High Performance Computing and Communications, 2014 IEEE 6th Intl Symp on Cyberspace Safety and Security, 2014 IEEE 11th Intl Conf on Embedded Software and Syst (HPCC, CSS, ICESS), 2014 IEEE Intl Conf on.

Li, Q., Unger, A., Sudicky, E., Kassenaar, D., Wexler, E., & Shikaze, S. (2008). Simulating the multi-seasonal response of a large-scale watershed with a 3D physically-based hydrologic model. *Journal of Hydrology*, *357*(3-4), 317–336. https://doi.org/10.1016/j.jhydrol.2008.05.024

Liu, G., Schwartz, F. W., Wright, C. K., & McIntyre, N. E. (2016). Characterizing the climate-driven collapses and expansions of wetland habitats with a fully integrated surface–subsurface hydrologic model. *Wetlands*, *36*(S2), 287–297. https://doi.org/10.1007/s13157-016-0817-9

Marzadri, A., Tonina, D., Bellin, A., & Tank, J. (2014). A hydrologic model demonstrates nitrous oxide emissions depend on streambed morphology. *Geophysical Research Letters*, *41*, 5484–5491. https://doi.org/10.1002/2014GL060732

Mattle, N., Kinzelbach, W., Beyerle, U., Huggenberger, P., & Loosli, H. (2001). Exploring an aquifer system by integrating hydraulic, hydrogeologic and environmental tracer data in a three-dimensional hydrodynamic transport model. *Journal of Hydrology*, *242*(3-4), 183–196. https://doi.org/10.1016/S0022-1694(00)00394-2

Miller, R., Heeren, D. M., Fox, G. A., Halihan, T., & Storm, D. E. (2016). Heterogeneity influences on stream water–groundwater interactions in a gravel-dominated floodplain. *Hydrological Sciences Journal*, *61*(4), 741–750. https://doi.org/10.1080/02626667.2014.992790

Mutiti, S., & Levy, J. (2010). Using temperature modeling to investigate the temporal variability of riverbed hydraulic conductivity during storm events. *Journal of Hydrology*, *388*(3–4), 321–334. https://doi.org/10.1016/j.jhydrol.2010.05.011

Nowinski, J. D., Cardenas, M. B., & Lightbody, A. F. (2011). Evolution of hydraulic conductivity in the floodplain of a meandering river due to hyporheic transport of fine materials. *Geophysical Research Letters*, *38*, L01401. https://doi.org/10.1029/2010GL045819

Pai, H., Malenda, H., Briggs, M., Singha, K., González-Pinzón, R., Gooseff, M., & Tyler, S. (2017). Potential for small unmanned aircraft systems applications for identifying groundwater-surface water exchange in a meandering river reach. *Geophysical Research Letters*, *44*, 11,868–11,877. https://doi.org/10.1002/2017GL075836

Partington, D., Therrien, R., Simmons, C. T., & Brunner, P. (2017). Blueprint for a coupled model of sedimentology, hydrology, and hydrogeology in streambeds. *Reviews of Geophysics*, *55*, 287–309. https://doi.org/10.1002/2016RG000530

Pasetto, D., Camporese, M., & Putti, M. (2012). Ensemble Kalman filter versus particle filter for a physically-based coupled surface-subsurface model. *Advances in Water Resources*, *47*, 1–13. https://doi.org/10.1016/j.advwatres.2012.06.009

Remy, N., Boucher, A., & Wu, J. (2009). *Applied geostatistics with SGeMS: A user's guide*. Cambridge: Cambridge University Press.

Ryan, R. J., & Boufadel, M. C. (2006). Influence of streambed hydraulic conductivity on solute exchange with the hyporheic zone. *Environmental Geology*, *51*(2), 203–210. https://doi.org/10.1007/s00254-006-0319-9

Schilling, O. S., Doherty, J., Kinzelbach, W., Wang, H., Yang, P., & Brunner, P. (2014). Using tree ring data as a proxy for transpiration to reduce predictive uncertainty of a model simulating groundwater–surface water–vegetation interactions. *Journal of Hydrology*, *519*, 2258–2271. https://doi.org/10.1016/j.jhydrol.2014.08.063

Schilling, O. S., Gerber, C., Partington, D. J., Purtschert, R., Brennwald, M. S., Kipfer, R., et al. (2017). Advancing physically-based flow simulations of alluvial systems through atmospheric noble gases and the novel 37Ar tracer method. *Water Resources Research*, *53*, 10,465–10,490. https://doi.org/10.1002/2017WR020754

Schilling, O. S., Irvine, D. J., Hendricks Franssen, H. J., & Brunner, P. (2017). Estimating the spatial extent of unsaturated zones in heterogeneous river-aquifer systems. *Water Resources Research*, *53*, 10,583–10,602. https://doi.org/10.1002/2017WR020409

Schomburg, A., Schilling, O. S., Guenat, C., Schirmer, M., Le Bayon, R. C., & Brunner, P. (2018). Topsoil structure stability in a restored floodplain: Impacts of fluctuating water levels, soil parameters and ecosystem engineers. *Science of the Total Environment*, *639*, 1610–1622. https://doi.org/10.1016/j.scitotenv.2018.05.120

Schubert, J. (2006). Experience with riverbed clogging along the Rhine River. In *Riverbank filtration hydrology* (pp. 221–242). Netherlands: Springer.

Shope, C. L., Constantz, J. E., Cooper, C. A., Reeves, D. M., Pohll, G., & McKay, W. A. (2012). Influence of a large fluvial island, streambed, and stream bank on surface water-groundwater fluxes and water table dynamics. *Water Resources Research*, *48*, W06512. https://doi.org/10.1029/2011WR011564

Simpson, S. C., & Meixner, T. (2012). Modeling effects of floods on streambed hydraulic conductivity and groundwater-surface water interactions. *Water Resources Research*, *48*, W02515. https://doi.org/10.1029/2011WR011022

Song, J., Chen, X., Cheng, C., Summerside, S., & Wen, F. (2007). Effects of hyporheic processes on streambed vertical hydraulic conductivity in three rivers of Nebraska. *Geophysical Research Letters*, *34*, L07409. https://doi.org/10.1029/2007GL029254

Song, J., Jiang, W., Xu, S., Zhang, G., Wang, L., Wen, M., et al. (2016). Heterogeneity of hydraulic conductivity and Darcian flux in the submerged streambed and adjacent exposed stream bank of the Beiluo River, northwest China. *Hydrogeology Journal*, *24*(8), 2049–2062. https://doi.org/10.1007/s10040-016-1449-0

Spreafico, M., & Weingartner, R. (2005). *The hydrology of Switzerland: Selected aspects and results*. Bern, Switzerland: Bundesamt für Wasser und Geologie.

Swisstopo. (2010). Bundesamt für Landestopografie swisstopo - swissALTI3D - Das hoch aufgelöste Terrainmodell der Schweiz, Bern, Switzerland.

Tang, Q., Kurtz, W., Brunner, P., Vereecken, H., & Franssen, H.-J. H. (2015). Characterisation of river–aquifer exchange fluxes: The role of spatial patterns of riverbed hydraulic conductivities. *Journal of Hydrology*, *531*, 111–123. https://doi.org/10.1016/j.jhydrol.2015.08.019

Tang, Q., Kurtz, W., Schilling, O., Brunner, P., Vereecken, H., & Franssen, H.-J. H. (2017). The influence of riverbed heterogeneity patterns on river-aquifer exchange fluxes under different connection regimes. *Journal of Hydrology*, *554*, 383–396. https://doi.org/10.1016/j.jhydrol.2017.09.031

Therrien, R., McLaren, R., Sudicky, E., & Panday, S. (2010). HydroGeoSphere: A three-dimensional numerical model describing fully-integrated subsurface and surface flow and solute transport. In *Groundwater simulations group* (pp. 9–28). Waterloo, ON: University Of Waterloo.

Tonina, D., & Buffington, J. M. (2007). Hyporheic exchange in gravel bed rivers with pool-riffle morphology: Laboratory experiments and three-dimensional modeling. *Water Resources Research*, *43*, W01421. https://doi.org/10.1029/2005WR004328

Ulrich, C., Hubbard, S. S., Florsheim, J., Rosenberry, D., Borglin, S., Trotta, M., & Seymour, D. (2015). Riverbed clogging associated with a California riverbank filtration system: An assessment of mechanisms and monitoring approaches. *Journal of Hydrology*, *529*, 1740–1753. https://doi.org/10.1016/j.jhydrol.2015.08.012

Van Genuchten, M. T. (1980). A closed-form equation for predicting the hydraulic conductivity of unsaturated soils. *Soil Science Society of America Journal*, *44*(5), 892–898. https://doi.org/10.2136/sssaj1980.03615995004400050002x

Wildhaber, Y. S., Michel, C., Epting, J., Wildhaber, R., Huber, E., Huggenberger, P., et al. (2014). Effects of river morphology, hydraulic gradients, and sediment deposition on water exchange and oxygen dynamics in salmonid redds. *Science of the Total Environment*, *470*, 488–500.

Woessner, W. W. (2000). Stream and fluvial plain ground water interactions: Rescaling hydrogeologic thought. *Ground Water*, *38*(3), 423–429. https://doi.org/10.1111/j.1745-6584.2000.tb00228.x

Würsten, M. (1991). *GWB - Hydrogeologische Untersuchungen Aeschau: Schlussbericht*. Zürich: Geotechnisches Institut.

Zhang, J., Song, J., Long, Y., Zhang, Y., Zhang, B., Wang, Y., & Wang, Y. (2017). Quantifying the spatial variations of hyporheic water exchange at catchment scale using the thermal method: A case study in the Weihe River, China. *Advances in Meteorology*, *2017*.

Zhang, Y., Hubbard, S., & Finsterle, S. (2011). Factors governing sustainable groundwater pumping near a river. *Groundwater*, *49*(3), 432–444. https://doi.org/10.1111/j.1745-6584.2010.00743.x